

Structure and Electrocatalytic Activity of Carbon-Supported Pt–Ni Alloy Nanoparticles Toward the Oxygen Reduction Reaction

Hui Yang, Walter Vogel,[†] Claude Lamy, and Nicolás Alonso-Vante*

Laboratory of Electrocatalysis, UMR CNRS 6503, University of Poitiers, 40 Avenue du Recteur Pineau, F-86022 Poitiers Cedex, France, and Fritz-Haber-Institut der Max-Planck-Gesellschaft, Faradayweg 4-6, 14195 Berlin, and Fachhochschule Brandenburg, Germany

Received: March 3, 2004; In Final Form: May 6, 2004

Vulcan XC-72 carbon-supported Pt–Ni alloy nanoparticle catalysts with different Pt/Ni atomic composition were prepared via the carbonyl complex route and their structure was studied by X-ray diffraction spectroscopy at wide angles (WAXS) and Debye function analysis (DFA). The very good agreement between the WAXS pattern and DFA simulation revealed that all the as-prepared Pt–Ni alloy catalysts have a unique and highly disordered face-centered cubic structure (solid solution) and that the lattice parameter decreases with the increase of the Ni content in the alloys. Transmission electron microscopy (TEM) images indicated that the as-prepared Pt–Ni alloy nanoparticles were well dispersed on the surface of the carbon support with a narrow particle size distribution and that their mean particle size slightly decreased with the increase in Ni content. Energy-dispersive X-ray analysis (EDX) confirmed that the catalyst composition was nearly the same as that of the nominal value. Thus, a comparative study was made for the oxygen reduction reaction (ORR) using the thin-film rotating ring-disk electrode method to the behavior of Pt based catalysts on the same carbon support, having the same metal loading, the same disordered structure, and a similar particle size. As compared to the Pt/C catalyst, the bimetallic catalysts with different Pt/ Ni atomic ratios exhibited an enhancement factor of ca. 1.5 to 3 in the mass activity and of ca. 1.5 to 4 in the specific activity for the ORR and a lower production of hydrogen peroxide in pure perchloric acid solution. The maximum activity of the Pt-based catalysts was found with ca. 30 ~ 40 at. % Ni content in the alloys, which could originate from the favorable Pt–Pt interatomic distance. The ring-current measurements on all the catalysts showed similar behavior for hydrogen peroxide production. The enhanced electrocatalytic activity of as-prepared Pt–Ni alloy catalysts for the ORR is attributed to the high dispersion of the alloy catalysts, to their disordered structure, and to the favorable Pt–Pt mean interatomic distance caused by alloying.

1. Introduction

Proton exchange membrane fuel cells (PEMFCs) have received considerable attention for applications in transportation, portable electronics, residential power sources, etc., due to their high energy density, relatively low operating temperatures, zero or low emission of pollutants, and minimal corrosion problems. However, the commercial viability of PEMFCs is still hindered by several factors, including the poor kinetics of the cathodic reaction^{1–4} and the high costs of both the polymer electrolyte membrane and the Pt-based electrocatalysts. It is well known that most of the performance losses from the thermodynamic potential in the PEMFC are due to the slow cathode kinetics. Thus, there is great room for improvement in oxygen reduction kinetics. In fact, the development of a more active oxygen reduction electrocatalyst than Pt has been the subject of extensive research for a number of decades.

Aiming to increase the catalytic activity of the oxygen reduction reaction (ORR) and to lower the cost of the catalysts, various Pt-based alloy catalysts, such as Pt–M (where M = Co, Ni, Fe, V, Mn, and Cr), have been studied for the last two decades.^{5–21} Generally, most of the authors reported an activity enhancement of the ORR on the alloy catalysts by factors of

1.5 to 3 in comparison to pure Pt. The improvement in the ORR electrocatalysis on Pt alloy catalysts has been explained by several factors, such as electronic and structural effects.^{9,11,15} Jalan and Taylor⁵ investigated Pt-based alloy catalysts for the ORR and suggested that the enhanced electrocatalytic activity is due to the shortening of the Pt–Pt mean interatomic distance. Mukerjee and Srinivasan⁸ and Min et al.¹¹ reported an ORR activity enhancement by a factor of 1.1 to 3 on several binary Pt–M (3:1) alloy catalysts. Such an activity enhancement was explained by an increase in the Pt d-band vacancy (electronic factor) and by the favorable Pt–Pt mean interatomic distance (geometric effect).^{9–11} Paffet et al.¹² reported that the ORR activity enhancement on the alloys could be ascribed to the surface roughening. Toda et al.¹⁴ investigated the effect of Pt alloying with Ni, Co, and Fe, prepared by sputtering, on the ORR activity and found enhancement factors of 10, 15, and 20 with 30, 40, and 50 at. % Ni, Co, and Fe, respectively. They attributed such significant enhancement factors to an increase in the Pt d-electron vacancy of the thin Pt skin layer caused by the underlying alloy. More recently, both carbon-supported¹⁷ and polycrystalline bulk¹⁸ Pt–Ni and Pt–Co catalysts were investigated for the ORR. In comparison to pure Pt, an activity enhancement by a factor of 1.5 to 3 was found, which is much lower than that observed by Toda et al.¹⁴ Thus, it should be pointed out that these results on the Pt alloy catalysts for the ORR are by no means consistent. Furthermore, Glass et al.⁶

* Corresponding author. Tel: +33-5-49-45-36-25. Fax: +33-5-49-45-35-80. E-mail: Nicolas.Alonso.Vante@univ-poitiers.fr.

[†] Fritz-Haber-Institut der Max-Planck-Gesellschaft.

reported that the Pt–Cr alloy for the ORR is less active than pure Pt in phosphoric acid media due to the bulk nature of the electrodes used in their study. Beard and Ross⁷ found that the specific activity of the Pt–Co alloy is lower than that of pure Pt and that the stability is not as good as that of pure Pt. This can be due to the particle size effect between Pt and Pt–Co alloy catalysts. Thus, when comparing the activity of Pt and Pt alloy catalysts, they pointed out that the effect of the particle size of the alloy catalysts should be taken into account. From the data reported in the literature, it is clear that the catalytic behavior of such Pt alloy catalysts for the ORR must be strongly influenced by the bulk and/or surface composition, the microscopic nature of the structure, and the local arrangement of atoms in the metallic core of the bimetallic nanoparticles. From this viewpoint, it is necessary to investigate the effect of such characteristics of the alloy catalysts with different Pt/M atomic ratios on the ORR and to correlate them to the catalytic activity.

Usually, carbon-supported Pt alloy catalysts are prepared by the impregnation of the second metal on Pt/C, and then by alloying at temperatures above 700 °C under an inert gas or hydrogen. This heat treatment at high temperatures gives rise to an undesired alloy particle growth, which may result in the decrease in Pt mass activity for the ORR since the mass activity (MA) of highly dispersed Pt catalysts decreases for particle sizes > 3.5 nm (surface-to-volume ratio generally decreases with radius, r^{-1}). The control of the particle size distribution with this preparation method is also quite limited. An alternative way to tailor the nanosized Pt-based alloys with small particle size and narrow size distribution for different purposes is the use of organometallic compounds as precursors. Among the various organometallic precursors used, metal carbonyl complexes are often employed for preparing carbon-supported metal or alloy catalysts. By the thermal decomposition of Ru carbonyl precursor in different organic solvents, Alonso-Vante²¹ and Dassenoy et al.²² synthesized Ru-based transition metal chalcogenide cluster-like nanomaterials for the ORR in pure and methanol-containing electrolytes. By reduction of the Pt–Ru carbonyl molecular precursors, Nasher et al.²³ and Hills et al.²⁴ prepared carbon-supported bimetallic Pt–Ru alloys with very small particle size and narrow size distribution. More recently, Dickinson et al.²⁵ synthesized carbon-supported Pt–Ru alloy catalysts by decomposing the Pt carbonyl and Ru carbonyl complexes in organic solvents. The obtained Pt–Ru catalysts with small particle size and narrow size distribution exhibited good performance for methanol oxidation in comparison to the commercial E-TEK Pt–Ru/C catalyst. Recently, our Laboratory successfully developed Pt–Sn²⁶ and Pt–Cr²⁷ alloy catalysts through the carbonyl complex route. The obtained alloy catalysts with small particle size, narrow size distribution, and disordered structure exhibited very good performance for electrocatalytic reactions.

It is known that the dispersion and the composition homogeneity of the alloy nanoparticles are also important factors to obtain a good electrocatalytic activity. In this work, carbon-supported Pt–Ni alloy nanoparticle catalysts with different Pt/Ni atomic ratios were prepared via the carbonyl complex route. To the best of our knowledge, this way of synthesizing Pt–Ni catalyst is new. The as-prepared catalysts were characterized by various physical and electrochemical techniques. X-ray diffraction spectroscopy at wide angles (WAXS) and Debye function analysis (DFA) were employed to evaluate the structural uniqueness of the alloy catalysts. Electrocatalytic activity of such as-prepared Pt–Ni alloy nanoparticle catalysts for the ORR was investigated and the possible influence of the catalyst

composition and structural parameters on the kinetics of the ORR was examined.

2. Experimental Section

2.1 Preparation of Carbon-Supported Pt–Ni Alloy Nanoparticle Catalysts. The nanosized Pt–Ni alloy catalysts were prepared via the carbonyl complex route, followed by H₂ reduction in the temperature range from 200 to 500 °C. In short, Pt and Ni carbonyl complexes were synthesized simultaneously using methanol as solvent through the reaction of Pt and Ni salts with CO at about 55 °C for 24 h with constant mechanical stirring until the solution turned green.^{28,29} The amount of sodium acetate added to the mixture was adjusted so that the sodium acetate/Pt molar ratio was 6 to 1. The synthesized carbonyl complexes were identified by infrared spectroscopy (Magna-IRTM Spectrometer 750, Nicolet) with a FTIR demountable path length cell (FT04–035/036, Spectra-Tech, Inc.) and the resultant product is probably a Pt–Ni molecular complex. After the synthesis of Pt–Ni carbonyl complexes, Vulcan XC-72 carbon was added to the mixture under N₂ gas flow and stirred at about 55 °C for more than 6 h. When the carbon powder was added to the mixture, the green color completely disappeared within a few minutes. This process seems to result in the bonding of Pt–Ni to the surface of carbon via a surface reaction and may favor a stronger interaction with the carbon support. Subsequently, the solvent was removed and the catalyst powder was subjected to heat treatment at different temperatures under nitrogen and hydrogen, respectively. The alloying temperature under hydrogen ranged from 200 to 500 °C. After heat treatment, the sample was washed with water until no chlorine ions were detected and then dried under nitrogen at about 130 °C. For the sake of comparison, the total metal loading of all the carbon-supported catalysts was about 20 wt. %.

2.2 Physical Characterization of the Nanosized Pt–Ni Alloy Catalysts. The particle size of the as-prepared catalysts was evaluated by transmission electron microscopy (TEM) using a Philips CM120 microscope equipped with a LaB₆ filament. The samples were prepared by placing one drop of the carbon-supported catalyst, which was dispersed in ethanol, on a copper grid covered by a carbon film and by evaporating the solvent. The particle composition of the as-prepared alloy catalysts was examined by EDX analysis with the microscope using the E-TEK Pt–Ni(1:1,10 wt %)/C catalyst as a reference. X-ray diffraction measurements were carried out on a Guinier powder diffractometer (Huber), set at a 45° transmission angle using the Cu–K α_1 radiation ($\lambda = 0.15406$ nm). The sample containing ca. 20 mg of catalyst was slightly pressed to a thin pellet of ~ 0.3 mm thickness. This pellet was then fixed between two 3 μ m polyethylene foils into the sample holder. The WAXS patterns were obtained with high-resolution in the step-scanning mode with a narrow receiving slit (0.125°). Scans were recorded in the theta-range of 5–48° at room temperature. The background-corrected spectra were subjected to the usual angular correction for absorption, polarization, and geometric factors, and plotted versus the reciprocal scattering length $b = 2\sin \theta/\lambda$, where θ is the Bragg angle, and λ is the wavelength of the X-ray radiation. Numerical simulation of the experimental data was performed with the help of DFA, which yields information on the intrinsic structure of the nanoparticles and on the size distribution of the assembly of coherently scattering nanoparticles within the clusters. This is achieved by comparing the linear combination of Debye functions of a sequence of model particles of different sizes and structures with the experimental data using a nonlinear least-squares parameter fit. A more detailed description of the DFA can be found in Vogel and co-workers.³⁰

2.3 Electrode Preparation and Electrochemical Measurements. Porous electrodes were prepared as described previously.³¹ Twenty mg of catalyst, 0.5 mL of Nafion solution (5 wt. %, Aldrich), and 2.5 mL of ultrapure water (MilliQ, Millipore) were mixed ultrasonically. A measured volume (3 μ L) of this ink was transferred via a syringe onto a freshly polished glassy carbon disk (3 mm in diameter). After the solvent was evaporated overnight at room temperature, the electrode was used as the working electrode. A previous study has proved that this method is reproducible and that the utilization of the Pt surface area is close to 100%.³¹ Each electrode contained about 56 μ g cm^{-2} of the metal catalyst.

All chemicals used were of analytical grade. All the solutions were prepared with ultrapure water (MilliQ, Millipore). Electrochemical measurements were performed using an Autolab Potentiostat/Galvanostat and a conventional three-electrode electrochemical cell. The counter electrode was a glassy carbon plate and a Mercury/Mercurous sulfate electrode (MSE) was used as the reference electrode, which was connected to the working electrode compartment by a Luggin capillary. All the potentials are quoted with respect to the reversible hydrogen electrode (RHE). Due to slight contamination from the Nafion solution, the porous electrodes were cycled at 50 mV sec^{-1} between 0.05 and 1.02 V vs. RHE until reproducible cyclic voltammograms were obtained prior to any electrochemical measurements. The upper potential was set to ca. 1.0V/RHE so that the particle surface change could be avoided. The real surface area of the nanodivided Pt was determined by CO-stripping voltammetry at the scan rate of 20 mV sec^{-1} .³² The commonly accepted value is 0.484 mC cm^{-2} for platinum.³² The electrocatalytic activity for the ORR was measured with the rotating disk electrode (RDE) (Autolab speed control) and the rotating ring-disk electrode (RRDE) (Autolab PGSTAT30 Bipotentiostat/Galvanostat and Pine Instrument AFMSRX modulated speed rotator) mounted with a Pine Instrument AFDT22 electrode: platinum ring electrode (0.152 cm^2) and glassy carbon disk (0.126 cm^2) with a collection efficiency $N = 0.21$. The Pt-ring electrode was controlled potentiostatically at 1.2V/RHE where the detection of hydrogen peroxide is diffusion limited. High purity nitrogen or oxygen (Air Liquide) was used for deaeration of the solutions. During the measurements, a gentle nitrogen or oxygen flow was kept above the electrolyte surface. All the electrochemical experiments were performed in a thermostated cell at a temperature of $20 \pm 1^\circ\text{C}$.

3. Results and Discussion

3.1 Preparation and Physical Characterization of the Carbon-Supported Pt–Ni Alloy Nanoparticles. Figure 1 shows the infrared (IR) spectra of three selected carbonyl complexes synthesized with the same concentration of sodium acetate and under similar reaction conditions. From the IR spectrum of as-synthesized $[\text{Pt}_3(\text{CO})_6]_5^{2-}$ dianions, a very strong band located at 2058 cm^{-1} and another band located at 1874 cm^{-1} are found, which have nearly the same values as published results,²⁸ clearly indicating the presence of the complex $[\text{Pt}_3(\text{CO})_6]_5^{2-}$ dianions. From the IR spectrum of the assumed pure Ni carbonyl complex, only one band centered at 2045 cm^{-1} is found, suggesting that $\text{Ni}(\text{CO})_4$ or Ni carbonyl dianions can be synthesized under the same reaction conditions.^{29,33} From the IR spectrum of the Pt–Ni(2:1) carbonyl complex, a strong broad band centered at 2050 cm^{-1} , and two weak bands located at 1824 and 1877 cm^{-1} are found. The strong band is likely due to the overlap of the Pt and Ni carbonyl complexes. However, these data are not conclusive to identify the molecular

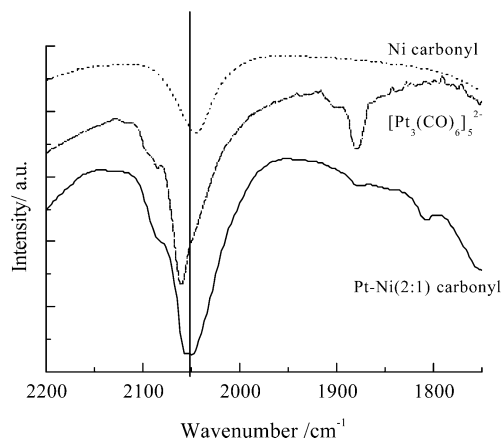


Figure 1. Infrared spectra of as-synthesized $[\text{Pt}_3(\text{CO})_6]_5^{2-}$ dianions, Ni–Carbonyl and Pt–Ni carbonyl complexes in methanol solution.

carbonyl precursor, for example, $(\text{Pt–Ni})_x(\text{CO})_y$ in comparison to platinum and nickel carbonyls. Therefore, the following cyclic voltammetry experiments were performed and gave some indication as to its chemical nature. We put some of the as-synthesized Pt–Ni carbonyl solution on the surface of a glassy carbon (GC) disk and then exposed it to air for more than 1 day. Subsequently, such a modified electrode was cycled between 0.05 and 1.02 V/RHE at 50 mVs^{-1} in N_2 -saturated perchloric acid solution. Surprisingly, the CO oxidation peaks can be found in the first several cycles, clearly indicating that at least some of the CO species are still bonded to the metal centers. However, when we put some pure Pt or pure Ni carbonyl solution on the surface of GC and then followed the same procedure, no CO oxidation peaks were found, probably due to the fact that on single-centered metal CO is more easily removed by air. In fact, previous studies proved that Pt–Ni–CO cluster complexes could be synthesized in organic media.³⁴ Based on this, it is assumed that the chemical precursor to prepare Pt–Ni alloy nanoparticle catalysts is a $(\text{Pt–Ni})_x(\text{CO})_y$ molecular complex. This assumption, however, needs more evidence (such as ^{13}C NMR and complex crystallographic structure analysis) to identify and to characterize the reaction intermediates and/or the resulting products in our synthesis procedure.

The atomic composition of the Pt–Ni alloy catalysts was evaluated by energy-dispersive X-ray (EDX) analysis but not nanoparticle point-resolved EDX. It was found that the EDX composition of a sample with a nominal atomic composition of 1:1 in various parts of the nanoparticle powder is about 52.0:48.0, which is very close to its nominal value. The obtained EDX compositions of all the alloy catalysts investigated in this work are given in Table 1. It can be seen that all the EDX compositions of the as-prepared Pt–Ni alloy catalysts are nearly the same as their nominal values. Evidence for alloying Ni with Pt through the carbonyl synthesis route is provided in section 3.2.

Figure 2 shows TEM images of carbon-supported Pt–Ni alloy catalysts with different Pt/Ni atomic ratios and the corresponding particle size distribution histograms based on the observation of more than 1000 nanoparticles. As can be seen, the Pt–Ni alloy nanoparticles are well dispersed on the surface of the carbon support with a narrow particle size distribution. The obtained average particle size and the standard deviation for all the catalysts are given in Table 1. In this table, we observe that the mean particle size of the as-prepared Pt–Ni alloy catalysts apparently decreases from 3.1 to 2.3 nm with the decrease of Pt/Ni atomic ratio from 5:1 to 1:1, suggesting that

TABLE 1: Composition and Mean Particle Size of the Pt/C (E-TEK) and As-prepared Pt–Ni/C Alloy Catalysts with 20 wt % Metal Loading

catalyst	EDX Pt/Ni composition (%)	particle size (nm) from TEM	dispersion D (%)	Pt real surface area (m ² g ^{−1})	Pt/Ni surface composition (%)
Pt/C(E-TEK)	(100)	2.8 ± 2.0 ^a	28.0	59.3	(100)
Pt:Ni(5:1)	84.1:15.9	3.1 ± 1.4	33.6	44.7	56:44
Pt:Ni(3:1)	73.9:26.1	2.8 ± 1.2	37.1	55.4	57:43
Pt:Ni(2:1)	65.8:34.2	2.4 ± 1.1	40.4	54.9	49:51
Pt:Ni(1:1)	52.0:48.0	2.3 ± 1.3	38.2	44.9	43:57

^a Obtained from Maillard et al.³¹

the addition of Ni species to the system seems to prevent, to a great extent, alloy particle aggregation during alloying. Due to a particle size heterogeneity, the carbon-supported platinum commercial catalyst (Pt/C E-TEK) shows a higher dispersion than the homemade Pt–Ni alloys. Assuming that all particles are spherical, the volume surface mean diameter (d_{vs}) of each catalyst sample could be obtained from the particle size distribution. Then, the surface average dispersion (D), which is defined as the ratio of the surface atoms to the total atoms within the nanoparticles, was also calculated using the relationship between relative particle size ($d_{rel} = d_{vs}/d_{at}$, where d_{at} is the atomic diameter) and D ($D = 2.64/(d_{rel})^{0.81}$) is based on the Borodzinski and Bonarowska model.³⁵ This model considers the particle size effects and is thus more accurate than other commonly used methods. The resulting D values for all catalysts are also given in Table 1. As can be seen in Table 1, all the alloy catalysts have higher dispersion than the Pt/C catalyst from E-TEK, which could be beneficial to the high MA for the ORR. In this work, the alloying temperature (≥ 200 °C) for the formation of Pt–Ni alloys via the carbonyl complex route is much lower than that of previously reported results.³⁶ Such a lower synthesis temperature together with a narrow size distribution could be favorable for the formation of small alloy nanoparticles. In fact, the mean particle size for all the Pt–Ni alloy catalysts prepared through the carbonyl route is smaller than that of E-TEK Pt–Ni alloy catalysts,¹⁷ assessing that the carbonyl complex route is an efficient method to obtain alloy nanoparticles with small particle size and narrow size distribution, and thus a good dispersion. This approach represents an advantage for scale production of alloy nanoparticles.

It is well-known that the real surface area of Pt within the catalyst is an important parameter to determine the electrocatalytic properties for the ORR. To evaluate the real surface area of Pt, the CO stripping voltammetry was employed according to the procedure described by Pozio et al.³² All the CO-stripping voltammograms of our nanodivided alloy catalysts presented one well-defined single CO oxidation peak. A typical example carried out on Pt–Ni (2:1)/C is shown in Figure 3. From the CO oxidation charge, the Pt real surface area of the Pt/C and Pt–Ni alloy catalysts was calculated and is also given in Table 1. The surface atomic density can be calculated by multiplying the total atomic density by the dispersion (cf. Table 1). From the surface atomic density and the electrochemically active surface area of Pt, the Pt/Ni surface composition of the alloy catalysts can be estimated and is given in Table 1. It was found that the Pt/Ni surface composition is lower than that of the EDX composition, indicative of the Ni enrichment of the alloy surface, which is similar to the Pt–Ni and Pt–Co alloy catalysts from E-TEK.^{17,18}

3.2 Structural Studies of the As-prepared Pt–Ni Alloy Nanoparticles. Figure 4 shows the XRD patterns (WAXS) of four prepared carbon-supported Pt–Ni alloy catalysts with a metal loading of 20 wt % and different Pt/Ni ratios, heat treated at 450 °C. All spectra are over-imposed by a line profile fitting

using five Pearson-VII type functions for the five observable Bragg peaks (111), (200), (220), (311), and (222) demonstrating that all the as-prepared alloy catalysts contain the single-phase disordered Pt *fcc*-structure (solid solution). No peak for pure Ni and its oxides was found. These five diffraction peaks in the Pt–Ni alloy catalysts are slightly shifted to higher theta values (or $b = 2\sin \theta/\lambda$) with respect to the corresponding peaks in the synthesized Pt sample (see the reference lines—dotted bars—of Pt in Figure 4 referring to the Joint Committee on Powder Diffraction Data (JCPDS-ICDD) database) and show the effect of increasing the amount of Ni in the Pt–Ni alloy catalysts. The higher angle shifts of the Pt peaks reveal the alloy formation between Pt and Ni, which was caused by the incorporation of Ni in the *fcc* structure of Pt. The five diffraction peaks allow a rather accurate determination of the mean lattice parameters. These parameters are shown in Figure 5 in comparison to data for the bulk alloy system of Pt and Ni.³⁷ The experimental values are plotted versus the nominal composition. A positive deviation from the bulk data with increasing Ni content is observed. This can be due either to (i) a lower Ni content than the nominal value, or (ii) an increasing lattice expansion with increasing Ni content in the alloy nanoparticles in relation to the bulk value. The latter explanation would be somehow surprising, since pure Pt nanoparticles are known to contract with decreasing size.^{38,39} (iii) A third possibility could be a nickel surface segregation. Such a phenomenon has been previously discussed for Pt–Ru nanoparticles.⁴⁰ The WAXS patterns in Figure 4 show an anomalous high intensity at the high angle wing of the first metal peak, which is, in fact, forming a halo-like slope for the Pt–Ni(2:1)/C sample. A fractional surface oxide that forms may explain this phenomenon, since the samples have been left exposed to air. The existence of some surface oxide on the air-exposed Pt–Ni alloy nanoparticles was verified by using a specially designed in situ XRD apparatus.⁴¹ The Pt–Ni(5:1)/C sample was kept between two 0.1 mm Be platelets under vacuum (10^{-3} mbar), and then exposed to 750 mbar of hydrogen. The intensity changes at the first peak of the metal phase ($\theta = 20^\circ \pm 1^\circ$, 111-peak), and at the low-angle wing of this peak ($\theta = 16^\circ \pm 1^\circ$), which is representative of surface oxides,^{30,41} were measured versus time and temperature. The two signals should show a reverse behavior due to the reduction of the surface oxide that leads to an increase of the fraction of the metal phase. This is in fact observed in Figure 6. At the point indicated by arrows the reaction cell is flushed with hydrogen at room temperature, which is followed by a rapid reduction, completed within ~ 2 min. No further reduction on increasing the temperature up to ~ 200 °C was seen. The slight increase of the signal at $\theta = 20^\circ$ is due to some small growth of the metal particles related to a narrowing of the metal peak.

We have performed a so-called Debye-Function-Analysis (DFA) of the diffraction data of the as-prepared Pt–Ni alloy samples. This method has been shown to be highly effective for the structural characterization of nanoparticle systems.^{22,30,39,42}

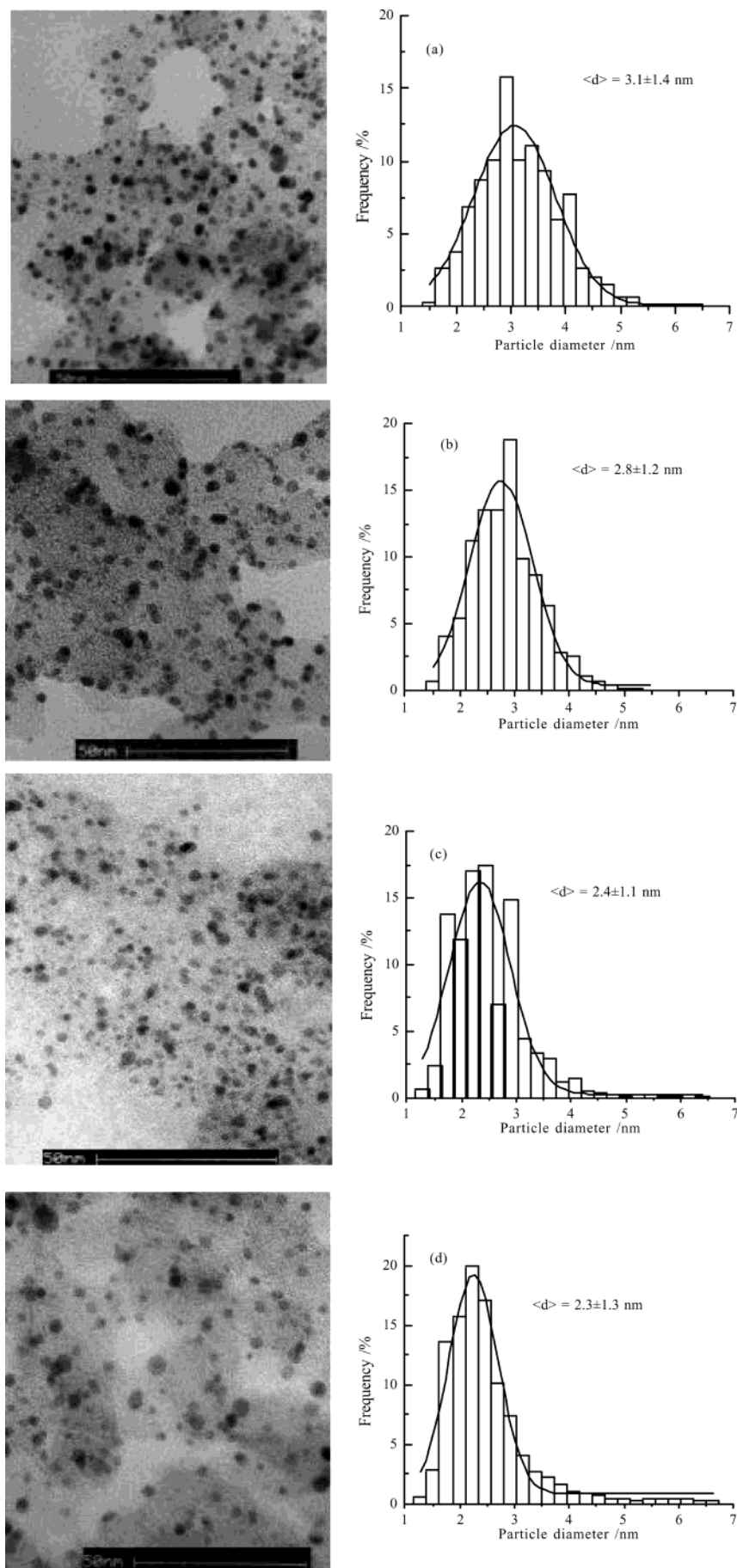


Figure 2. TEM images and the corresponding particle size distribution histograms of (a) Pt-Ni(5:1)/C, (b) Pt-Ni(3:1)/C, (c) Pt-Ni(2:1)/C, and (d) Pt-Ni(1:1)/C catalysts with 20 wt % metal loading.

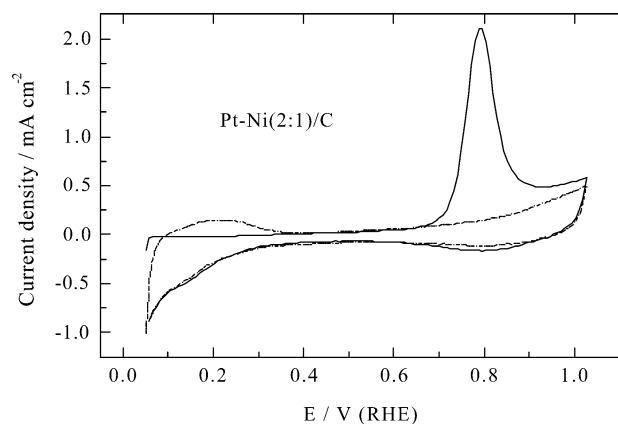


Figure 3. CO-stripping voltammogram of the Pt–Ni(2:1)/C catalyst in 0.5 M HClO₄ at a scan rate of 20 mV/s. Current density is normalized to the geometric surface area.

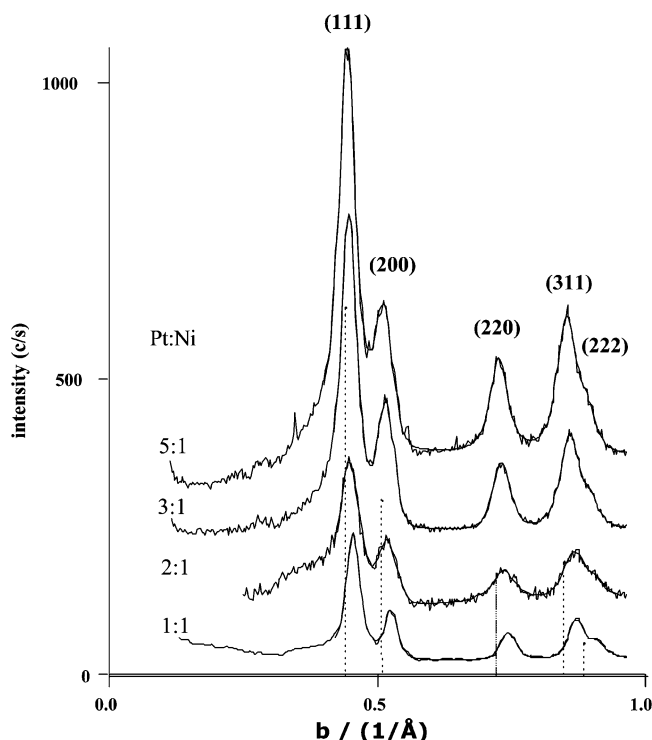


Figure 4. WAXS patterns shown with offsets of each by 100 (c/s) for Pt–Ni(5:1), (3:1), (2:1), and (1:1) carbon-supported catalysts with 20 wt % metal loading. The patterns are corrected for the background produced by Vulcan XC-72 support, and corrected for the usual angular factors: polarization, absorption, and geometrical factor. The high intensity at the left wing of the first peak is indicative of some fractional surface oxide. Reference lines for Pt are also shown in dotted bar.

Basically the method consists of a simulation of the experimental diffraction pattern by a linear combination of the intensity calculated for model particles (Debye functions). These model particles represent a system of particles that increase in size by addition of a new shell of surface atoms. Each of them is represented in the whole assembly by its frequency of occurrence, which is used as a free parameter in the DFA simulation. It also provides information on the symmetry by comparing different crystal structures (*fcc*, *hcp*, *bcc*, etc., or noncrystallographic icosahedral or decahedral structure). Frequently occurring planar defects such as stacking faults can be easily modeled. DFA will also allow the accurate determination of the mean interatomic distance in the nanoparticles.³⁹ Figure 7 shows the DFA performed on the Pt–Ni(5:1)/C carbon-supported nano-

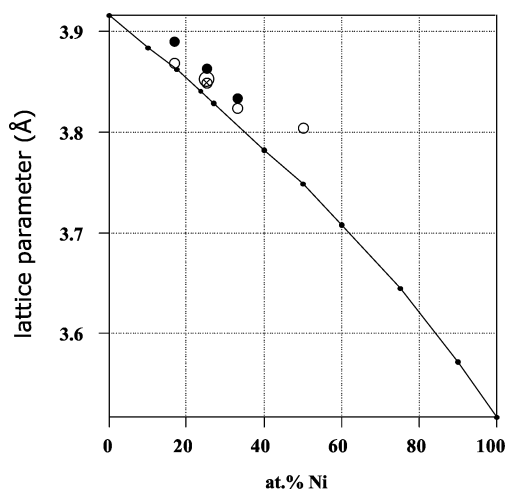


Figure 5. Experimental lattice parameters of the alloy nanoparticles compared with literature data for bulk PtNi alloys obtained by Esch and Schneider⁴⁰ (small filled circles). For each Pt–Ni composition, the experimental points (○, ●, ⊗) represent different complex syntheses.

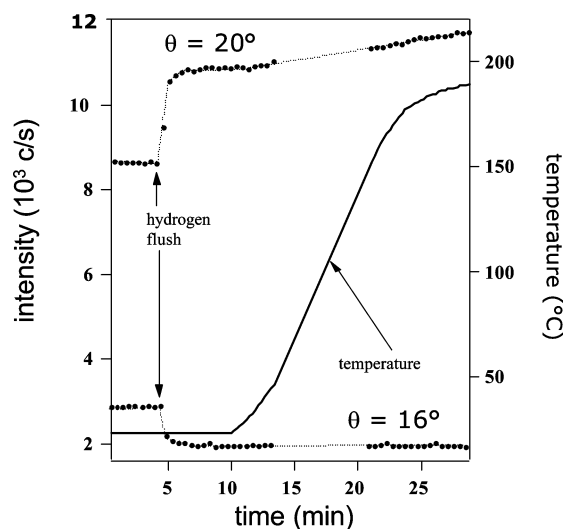


Figure 6. Surface oxide reduction via hydrogen flush followed by in situ XRD measurement as a function of temperature.

particle diffraction pattern. The best result was found for a system of twinned *fcc* particles, average lattice parameter $a = 3.889$ Å. The size distribution, weighted by the particle mass, is given in the insert of Figure 7. The volume average size is $d = 29$ Å (number average: 24 Å). However, there is a small mismatch with the experimental curve at high angles, which usually does not occur for monometallic systems. In addition, the size distribution used for modeling does not match well with that observed by TEM (see Figure 2a). Such a phenomenon may be related to some chemical inhomogeneity of the alloy particles that would be displayed as a broadening of the high-order peaks. In our simulation process, however, we have to assume that all alloy nanoparticles are exactly of the same composition. A remarkable effect is observed if we go to higher Ni loading: the DFA works better by using *fcc* model particles free of twinning defects. A typical effect of twinning is a broadening of the (200) peak correlated with a reduction of the peak height. As an example, Figure 8 shows the DFA for the Pt–Ni(3:1)/C, performed with perfect *fcc*-type model particles. This simulation became even better by adding a fraction of ~ 20 wt. % of small Pt₃O₄ particles to the model system, in agreement with the qualitative statement made above. However, as was the case for the Pt–Ni(5:1)/C, deviations are visible at

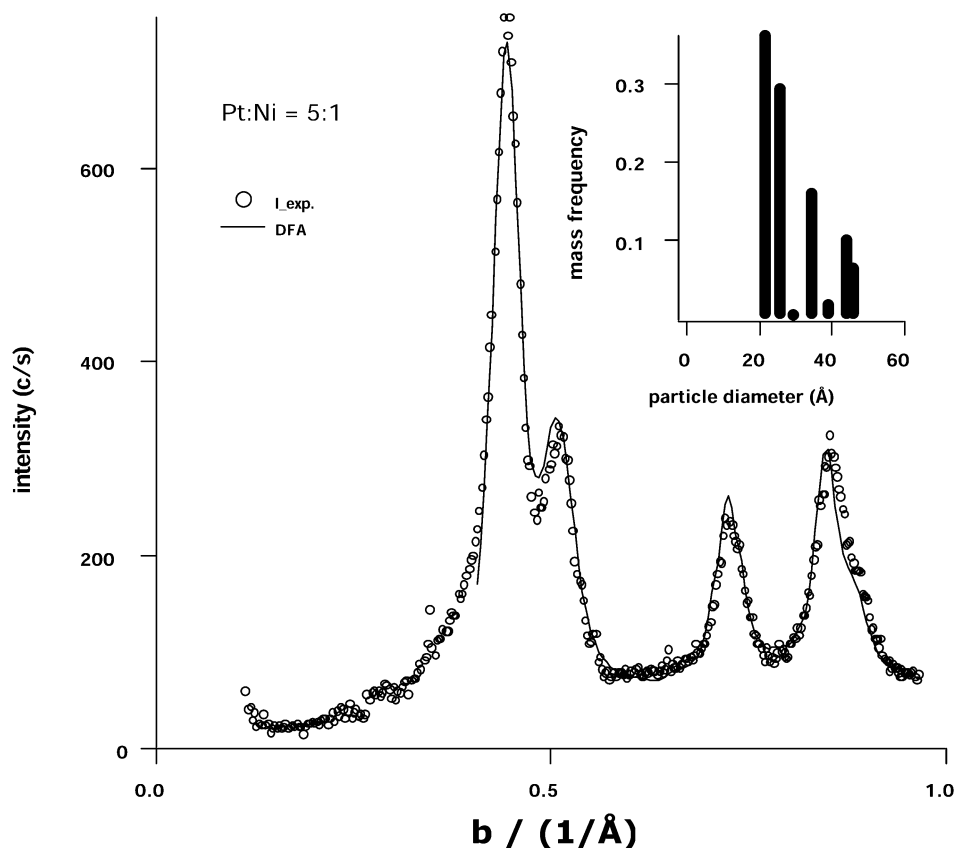


Figure 7. DFA of the Pt–Ni(5:1)/C alloy nanoparticles (solid line). The simulation is highly improved by using *fcc* model particles containing twin defects. The insert shows the mass fractions of the model particles used for the simulation versus their diameter.

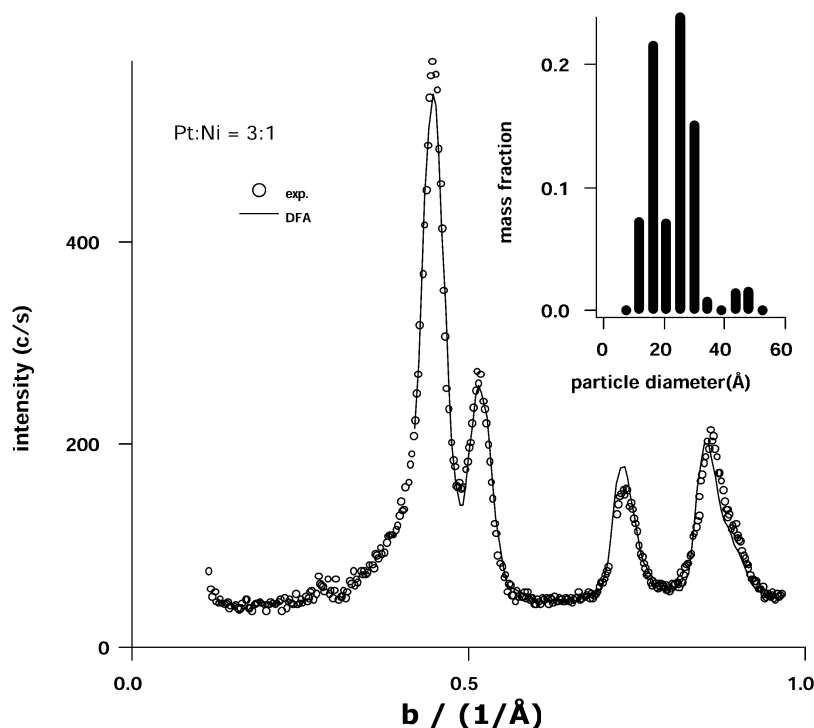


Figure 8. DFA of the Pt–Ni(3:1)/C alloy nanoparticles (solid line). The simulation is performed using *fcc* model particles containing no twin defects. The insert shows the mass fractions of the model particles used for the simulation versus their diameter.

the high order diffraction peaks (311) (222), most probably related to some incomplete alloying. The mean lattice parameter is 3.852 Å, and the mass/number-weighted mean size is 21/17 Å. The size distribution (see the insert of Figure 8) is in good agreement with the TEM result for this sample (Figure 2b). This similarity is better observed on the maximum of the frequency.

However, the distribution obtained by DFA is less accurate and this effect may produce a difference in the averaged values.

The XRD spectra of the other alloy samples were of lower quality and therefore not feasible for DFA with a meaningful accuracy. For comparison, we also investigated a commercial pure platinum catalyst supported on carbon, for example, Pt/

TABLE 2: Structural Parameters of the Pt Based Alloy Catalysts

catalyst	lattice parameters a_{fcc}/nm	Pt–Pt mean interatomic distance (nm)	particle size (nm) from WAXS	debye factor ^a $B/\text{\AA}^2$
Pt/C(E-TEK)	0.3923	0.2774	3.1	
Pt:Ni(5:1)/C	0.3889	0.2749	2.8	1.5
Pt:Ni(3:1)/C	0.3852	0.2724	2.8	1.4
Pt:Ni(2:1)/C	0.3824	0.2704	2.3	
Pt:Ni(1:1)/C	0.3803	0.2689	2.8	

^a B for Pt bulk is 0.3 \AA^2 .

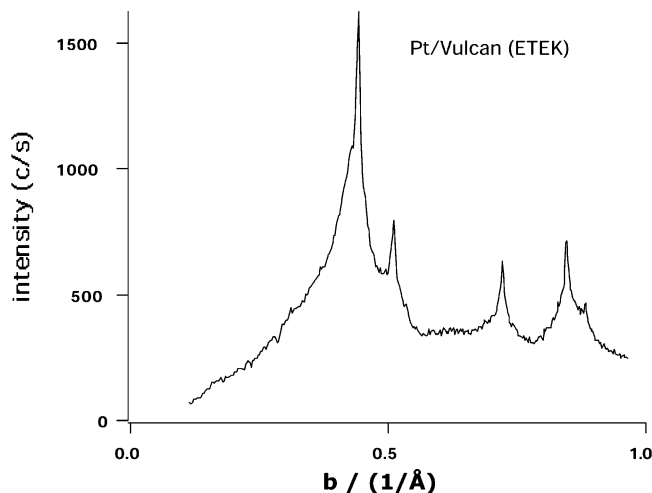


Figure 9. WAXS pattern of commercial Pt/Vulcan E-TEK catalyst. The background was corrected for the Vulcan support scattering and all angular factors.

Vulcan from E-TEK with 20 wt % loading. This pattern is shown in Figure 9. Apparently, this material is very heterogeneous, consisting of a (smaller) fraction of very large particles, estimated to be $> 80 \text{ \AA}$ in size. These particles produce the narrow peaks that are over-imposed onto a diffuse diffraction pattern from smaller Pt particles. Since XRD is mass sensitive, the fraction of small particles are in majority. The heterogeneity of this material makes a quantitative analysis impossible.

The lattice parameters (a_{fcc}) and Pt–Pt mean interatomic distance of Pt-based catalysts, as deduced from line profile analysis, are given in Table 2. The obtained lattice parameters and Pt–Pt mean interatomic distances for all the Pt–Ni alloy catalysts are smaller than those for E-TEK Pt/C catalyst and decrease with the increase of Ni content, indicating the lattice contraction after alloying. In fact, the decrease of the lattice parameter and of the Pt–Pt mean interatomic distance within the alloy catalysts reflects the conversion of Ni into the alloyed state. The nearly linear relationship between the lattice parameter and EDX composition analysis again confirmed that Ni is completely alloyed with Pt within all the as-prepared Pt–Ni alloy catalysts (data not shown). Thus, it can be concluded that the practical composition of the alloy catalysts is nearly similar to the nominal one and in agreement with the WAXS analysis.

The average size of the Pt–Ni alloy nanoparticles was also estimated by using Scherrer's equation:⁴³ $d = 0.94\lambda_{\text{K}\alpha 1}/\beta_{(2\theta)}\cos \theta_B$, where d is the average particle diameter, $\lambda_{\text{K}\alpha 1}$ is the wavelength of X-ray radiation (0.15406 nm), θ_B is the angle of the (220) peak, and $\beta_{(2\theta)}$ is the width in radians of the diffraction peak at half-height. The obtained average particle sizes of all the catalysts are given in Table 2. In addition, it is very interesting to note that all the XC-72 carbon-supported catalysts have nearly the same structure and similar particle size; thus, under these conditions it is suitable to compare their electrocatalytic activity for the ORR.

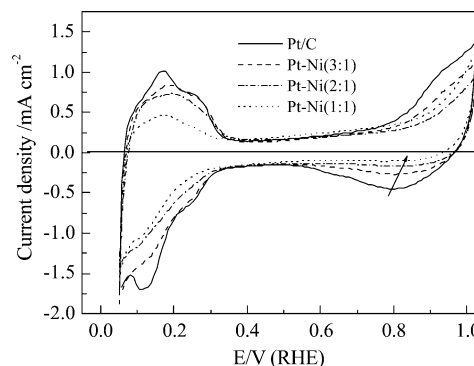


Figure 10. CVs of the Pt/C catalyst and carbon-supported Pt–Ni alloy nanoparticle catalysts in 0.5 M HClO_4 at the scan rate of 50 mV/s. Current densities are normalized to the geometric surface area.

3.3 Activity of the Pt–Ni Alloy Catalysts for the Oxygen Reduction Reaction.

Figure 10 shows the cyclic voltammograms (CVs) of the Pt/C catalyst and the selected carbon-supported nanosized Pt–Ni alloy catalysts in 0.5 M HClO_4 at the scan rate of 50 mV s^{-1} between 0.05 and 1.02 V/RHE. From the CV of the Pt/C catalyst in Figure 10, the hydrogen adsorption/desorption peaks and preoxidation/reduction peaks of the Pt surface are clearly seen, indicating the presence of polycrystalline Pt. But for the Pt–Ni alloy catalysts, no well-defined hydrogen adsorption/desorption peaks were found, suggesting that the high dispersion of the catalysts with a disordered surface structure was obtained and that no surface enrichment of platinum was found, which is similar to the estimated Pt/Ni surface composition (see Table 1). Additionally, it can be observed that the onset of the oxide formation and the peak potential of the oxide reduction (see arrow in the figure) are also shifted to more positive potentials with the increase in Ni content, indicating that the alloying of Pt with Ni inhibits the chemisorption of OH on the Pt sites at potentials above 0.8 V. This may have a beneficial effect on the oxygen adsorption at low overpotentials, and thus may lead to the enhancement of the ORR kinetics.^{10,18,44} It should be mentioned here that no marked changes in the shape and size of the CVs were observed throughout the electrochemical measurements and that the Pt real surface area of all the catalysts kept almost constant, indicating that the catalysts are stable and that no further Pt or Ni surface enrichment does occur under these experimental conditions. When cycling between 0.05 and 1.2 V/RHE, however, some changes in both the shape and size of the CVs are found, showing that possible changes in Pt real surface area and/or surface composition take place.

Figure 11 shows the ORR on the Pt/C and as-prepared Pt–Ni catalysts under the same experimental conditions at a low scan rate (5 mV s^{-1}). The rotating ring-disk electrode (RRDE) technique was additionally used for Pt/C, Pt–Ni(2:1)/C, and Pt–Ni(1:1)/C, respectively. From the figure, the ORR on all the catalysts is diffusion-controlled when the potential is less than 0.7 V/RHE and is under mixed diffusion-kinetics control

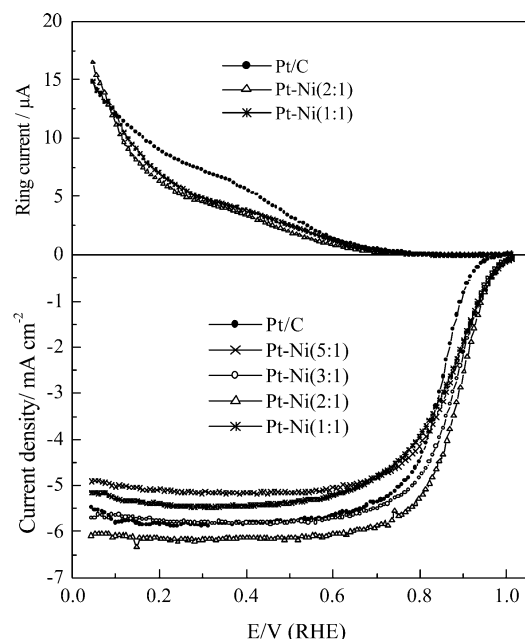


Figure 11. Linear scan voltammograms of the carbon-supported nanosized Pt and Pt–Ni alloy catalysts in 0.5 M HClO₄ saturated with pure oxygen (scan rate of 5 mV/s and rotating speed of 2000 rpm). Current densities are normalized to the geometric surface area. The ring currents, (RRDE) data, for the hydrogen peroxide production on Pt/C, Pt–Ni(2:1)/C and Pt–Ni(1:1)/C systems are also given.

in the potential region between 0.7 and 0.90 V. In the Tafel region (potentials higher than 0.90 V) and the mixed potential region, it was found that the catalytic activity of all Pt–Ni alloy catalysts toward the ORR is higher than that of pure Pt with respect to the MA referred to the total metal loading. Based on the MA of Pt, however, all the Pt–Ni alloy catalysts show an activity enhancement factor from 1.5 to 4 in comparison to the Pt/C catalyst for the ORR. The maximum activity was found with a Pt/Ni atomic composition of 2:1. From Figure 11, it is clear that the decrease in the overpotential of the ORR on Pt–Ni (2:1)/C catalyst at the same current density is at least 50 mV compared to that on a Pt/C catalyst. In this connection, RRDE data are also illustrative of the charge-transfer pathway (4e[−] water formation or 2e[−] hydrogen peroxide formation) of the ORR process on Pt compared to the homemade alloy catalysts. It is believed that such high enhancement factors in MA are ascribed to the high dispersion and the disordered structure of the as-prepared catalysts. Furthermore, the Koutecky–Levich plots (not shown) for the ORR on the different catalytic electrodes showed that all plots are straight lines with almost the same slope as that of the theoretically predicted line for a four-electron reduction of oxygen, indicating that the oxygen reduction on all Pt-based catalysts follows a four-electron process leading to water. From this figure, it can be seen that the ring currents amount to negligible fractions of the disk currents in the potentials above 0.70 V, indicating that the ORR proceeds without hydrogen peroxide production. The ring currents continuously increase starting from the potentials below 0.70 V. The amount of hydrogen peroxide production on all Pt–Ni alloy catalysts is roughly similar and is lower than that on pure Pt, which is different from E-TEK Pt–Ni(1:1)/C catalyst with a higher hydrogen peroxide yield.¹⁷ The fraction of hydrogen peroxide, $x_{\text{H}_2\text{O}_2}$, in the diffusion controlled region (0.3 V/RHE) was evaluated from the disk current, I_D , the ring current, I_R , and the collection factor, N , using the equation: $x_{\text{H}_2\text{O}_2} = 2(I_R/N)/(I_D + I_R/N)$.⁴⁵ The fractions are: 8.6%, 5.2%, and 6.4%

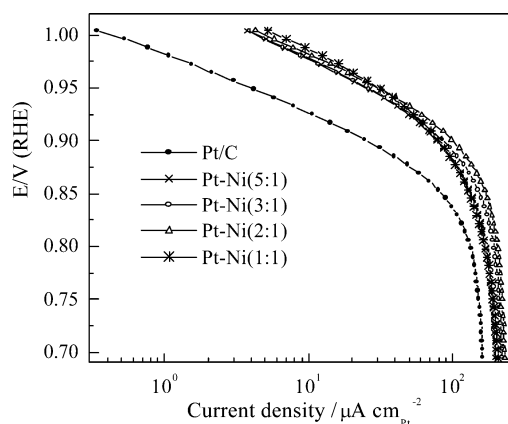


Figure 12. E vs $\log j$ plots for the ORR on the different Pt-based catalysts in 0.5 M HClO₄ (5 mV/s and 2000 rpm). Current densities are normalized to the real surface area of platinum within the catalysts.

for Pt/C, Pt–Ni(2:1)/C, and Pt–Ni(1:1)/C, respectively. It is worth mentioning that the open circuit potential of the Pt–Ni alloy catalysts in oxygen-saturated solution is about 30 mV higher than that of Pt/C catalyst, suggesting that the oxygen adsorption on the alloy surface is more favored than that on a pure Pt surface. Paulus et al.¹⁷ reported that the E-TEK Pt–Ni(1:1)/C catalyst is less active and unstable than the Pt catalyst at oxygen electrode potentials. The homemade Pt–Ni (2:3, 20 wt. %)/C catalyst with the simple-phase disordered structure was also examined for the ORR; its mass activity (MA) and specific activity (SA) values are higher than those of Pt/C alone. In addition, we also prepared a Pt–Ni(1:1)/C catalyst with a metal loading of 40 wt. %. In comparison to Pt/C catalyst (from E-TEK) with the same metal loading, the as-prepared alloy catalyst with a mean particle size of ca. 3.0 nm exhibited very good performance for the ORR in a Direct Methanol Fuel Cell (DMFC) operating between 50 °C and 100 °C.

To compare the specific activity of the different Pt-based catalysts for the ORR, E vs $\log j$ plots of the kinetic current densities based on the real surface area of platinum within the catalysts are shown in Figure 12. From the figure, the Tafel slope can be obtained. The obtained Tafel slopes at high potentials (> 0.90 V) for the Pt/C, Pt–Ni(5:1)/C, Pt–Ni(3:1)/C, Pt–Ni(2:1)/C, and Pt–Ni(1:1)/C catalysts are 59, 61, 63, 62, and 61 mV decade^{−1}, respectively. Within the fitting error, the Tafel slope did not show any dependence on the composition and structural parameters of the catalysts. Thus, it can be concluded that the reaction pathway and the rate-determining step are the same on all the catalysts investigated here. Furthermore, it is evident that the SA of the Pt–Ni alloy catalysts for the ORR is higher than that of the Pt/C catalyst and that the maximum SA was found with a Pt/Ni atomic composition of ca. 2:1. For example, the SA of Pt–Ni (2:1)/C for the ORR at 0.85 V/RHE and 0.90 V/RHE is ca. 2 and 4 times higher than that of the Pt/C catalyst, respectively. Generally, the kinetics enhancement in SA for the ORR on the homemade Pt–Ni alloy catalysts corresponds to a factor of 1.5 to 4, which depends on the catalyst composition and the polarization potential.

It is well-known that the change in surface composition or in Pt surface area of Pt-based catalysts may play an important role in the ORR electrocatalysis.⁴⁶ Thus, it is necessary to determine the possible changes in surface composition or surface segregation during the electrocatalytic process.¹⁸ The real surface area of Pt in the Pt–Ni alloy catalysts before and after the electrochemical polarization at 0.80 V for 1 h in oxygen-saturated perchloric acid solution increased only by ca. 3.5%,

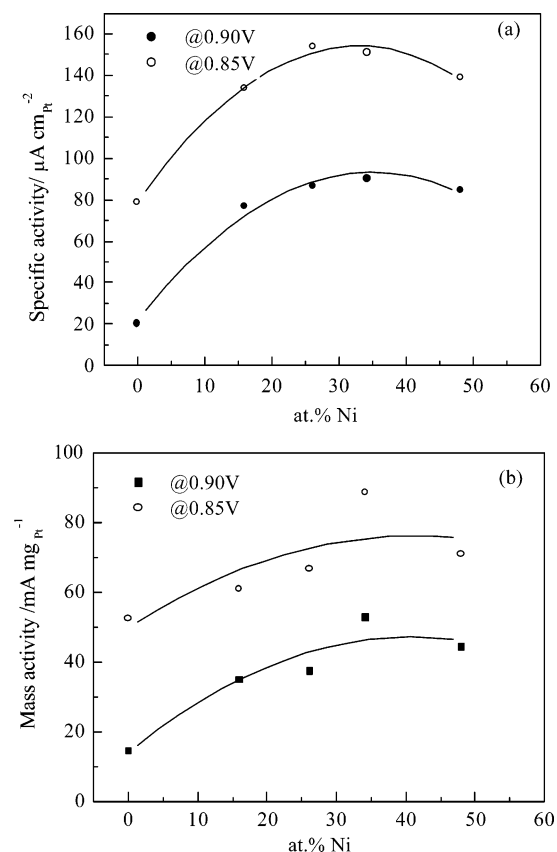


Figure 13. Relationship between the specific activity (a) and the mass activity (b) for the ORR in 0.5 M HClO_4 solution on Pt and homemade Pt–Ni alloy catalysts versus the nickel composition (at. % Ni).

indicating that the stability of the alloy catalyst is good and that no Pt surface enrichment on the alloy catalysts occurs during the ORR. Thus, it is believed that the Pt/Ni surface composition almost keeps a constant value during the electrochemical measurements. However, more spectroscopic work under in situ conditions is needed to assess this assumption.

The changes in SA and MA of the Pt–Ni alloy catalysts toward the ORR at 0.85 V and 0.90 V vs RHE are plotted as a function of the nickel amount (at. %) in Figures 13a and 13b. It is clear that all the Pt–Ni alloy catalysts present an activity enhancement for the ORR and the maximum activity is found with the Pt/Ni atomic composition between 30 and 40 at. % Ni, which is roughly similar to that obtained on sputtered Pt alloy skin films.¹⁴ In general, the activity enhancement for the ORR on Pt-based alloy catalysts could be ascribed to the changes in structural parameters (such as lattice parameter and Pt mean interatomic distance) and the Pt–M composition. Mukerjee and McBreen⁴⁷ studied the enhancement mechanism on some alloys for the ORR by using EXAFS and XANES techniques. They suggested that such an activity enhancement could be explained by the increased Pt d-band vacancy and by the favorable Pt–Pt mean interatomic distance of ca. 0.271 or 0.273 nm.^{9,10} Min et al.¹¹ and Antolini et al.¹⁹ also examined the relationship between the SA and the Pt–Pt interatomic distance of several alloy catalysts, and the maximum SA was found at a Pt–Pt interatomic distance of ca. 0.273 nm. Toda et al.¹⁴ found that the maximum activity for the ORR on the sputtered Pt alloy skin layer locates at the Pt–Pt neighbor distance of 0.271 to 0.275 nm. In our work, it can be seen that the maximum activity is found with the Pt/Ni atomic composition between 30 and 40 at. % Ni, corresponding to the Pt–Pt

mean interatomic distance of ca. 0.2704 to 0.2724 nm (see Table 2). Thus, it can be concluded that the high activity of these catalysts for the ORR comes from the favorable Pt–Pt mean interatomic distance caused by nickel alloying and the disordered surface structures induced by the particle size. Of course, a good dispersion of the Pt–Ni alloy catalysts as demonstrated in this work is also an important factor to determine their activity for the ORR.

Thus, the ORR kinetics, as summarized in Figures 13, display an enhanced electrocatalytic activity (both in SA and MA) in comparison to Pt alone. At 0.90 V, an enhancement factor of ca. 2 to 3 in MA and of ca. 3 to 4 in SA for the ORR on the alloy catalysts in perchloric acid solution was found as compared to the Pt/C catalyst. At 0.85 V, an enhancement factor of ca. 1.5 to 2 in both MA and SA for the ORR on the alloy catalysts was found when compared to the Pt/C catalyst. An enhancement factor of ca. 1.5 (both in MA and SA) on commercial Pt–Ni nanoparticle catalysts for the ORR was reported previously,^{8,17} the value of which is lower than that on our homemade alloy catalysts. Thus, the homemade Pt–Ni alloy catalysts with the disordered structure and well-dispersed nanoparticles on Vulcan XC-72 could be used in practical PEMFCs and DMFCs.

4. Conclusions

The oxygen reduction reaction on Vulcan XC-72 carbon-supported nanosized Pt–Ni alloy catalysts has been studied. The catalyst preparation procedure via the carbonyl complex route seems to be an efficient method to obtain Pt–Ni alloy nanoparticles of controlled atomic composition with a narrow particle size distribution and a disordered structure. It is believed that the precursor used for preparing the Pt–Ni alloy catalysts is a $(\text{Pt–Ni})_x(\text{CO})_y$ molecular complex. Compared with the Pt/C catalyst with similar metal loading, the same disordered *fcc* structure and similar particle size, the bimetallic catalysts with the different Pt/Ni atomic ratios showed an enhancement factor of ca. 1.5 to 3 in the mass activity and of ca. 1.5 to 4 in the specific activity for the ORR in perchloric acid solution. The maximum activity of the Pt based catalysts was found with ca. 30 ~ 40 at. % Ni content in the alloys, which could originate from the favorable Pt–Pt mean interatomic distance. The enhanced electrocatalytic activity of the as-prepared Pt–Ni alloy catalysts for the ORR is attributed to the high dispersion of the alloy catalysts, the disordered structure and the favorable Pt–Pt mean interatomic distance caused by alloying.

Acknowledgment. The authors greatly acknowledge the French Fuel Cell Network, and the Ministry of Research for their support in the framework of the OPTIMET program (research grant no. 00S0060). N. Alonso-Vante thanks the Alexander von Humboldt Stiftung and the Max Planck Gesellschaft for funding his stay at the Fritz-Haber-Institut, Berlin, Germany.

References and Notes

- (1) Arico, A.; Srinivasan, S.; Antonucci, V. *Fuel Cells* **2001**, 2, 133.
- (2) Ralph, T. R.; Hogarth, M. P. *Platinum Metals Rev.* **2002**, 46, 3.
- (3) Gottesfeld, S.; Raistrick, I. D.; Srinivasan, S. *J. Electrochem. Soc.* **1987**, 134, 1455.
- (4) Freund, F.; Lang, J.; Lehman, T.; Starz, K. A. *Catal. Today* **1996**, 27, 279.
- (5) Jalan, V.; Taylor, E. J. *J. Electrochem. Soc.* **1983**, 130, 2299.
- (6) Glass, G. T.; Cahen, G. L.; Stoner, G. E.; Taylor, E. J. *J. Electrochem. Soc.* **1987**, 134, 58.
- (7) Beard, B. C.; Ross, P. N. *J. Electrochem. Soc.* **1990**, 137, 3368.
- (8) Mukerjee, S.; Srinivasan, S. *J. Electroanal. Chem.* **1993**, 357, 201.
- (9) Mukerjee, S.; Srinivasan, S.; Soriaga, M. P. *J. Phys. Chem. B* **1995**, 99, 4577.

- (10) Mukerjee, S.; Srinivasan, S.; Soriaga, M. P.; McBreen, J. *J. Electrochem. Soc.* **1995**, *142*, 1409.
- (11) Min, M. K.; Cho, J.; Cho, K.; Kim, H. *Electrochim. Acta* **2000**, *45*, 4211.
- (12) Paffet, M. T.; Beery, G. J.; Gottesfeld, S. *J. Electrochem. Soc.* **1988**, *135*, 1431.
- (13) Kim, K. T.; Kim, Y. G.; Chung, J. S. *J. Electrochem. Soc.* **1995**, *142*, 1531.
- (14) Toda, T.; Igarashi, H.; Uchida, H.; Watanabe, M. *J. Electrochem. Soc.* **1999**, *146*, 3750.
- (15) Drillet, J. F.; Ee, A.; Friedemann, J.; Kötzt, R.; Schmidt, V. M. *Electrochim. Acta* **2002**, *47*, 1983.
- (16) Tamizhmani, G.; Capuano, G. A. *J. Electrochem. Soc.* **1994**, *141*, 968.
- (17) (a) Paulus, U. A.; Wokaun, A.; Scherer, G. G.; Schmidt, T. J.; Stamenkovic, V.; Markovic, N. M.; Ross, P. N. *J. Phys. Chem. B* **2002**, *106*, 4181. (b) Paulus, U. A.; Wokaun, A.; Scherer, G. G.; Schmidt, T. J.; Stamenkovic, V.; Markovic, N. M.; Ross, P. N. *Electrochim. Acta* **2002**, *47*, 3787.
- (18) (a) Stamenkovic, V.; Schmidt, T. J.; Ross, P. N.; Markovic, N. M. *J. Phys. Chem. B* **2002**, *106*, 11970. (b) Stamenkovic, V.; Schmidt, T. J.; Ross, P. N.; Markovic, N. M. *J. Electroanal. Chem.* **2003**, *554–555*, 191.
- (19) Antolini, E.; Passos, R. R.; Ticianelli, E. A. *Electrochim. Acta* **2002**, *48*, 263.
- (20) Shim, J.; Yoo, D. Y.; Lee, J. S. *Electrochim. Acta* **2000**, *45*, 1943.
- (21) Alonso-Vante, N. *J. Chem. Phys.* **1996**, *93*, 702.
- (22) Dassenoy, F.; Vogel, W.; Alonso-Vante, N. *J. Phys. Chem. B* **2002**, *106*, 12152.
- (23) Nasher, M. S.; Frenkel, A. I.; Somerville, D.; Hills, C. W.; Shapley, J. R.; Nuzzo, R. G. *J. Am. Chem. Soc.* **1998**, *120*, 8093.
- (24) Hills, C. W.; Nasher, M. S.; Frenkel, A. I.; Shapley, J. R.; Nuzzo, R. G. *Langmuir* **1999**, *15*, 690.
- (25) Dickinson, A. J.; Carrette, L. P. L.; Collins, J. A.; Friedrich, K. A.; Stimming, U. *Electrochim. Acta* **2002**, *47*, 3733.
- (26) (a) Manzo-Robledo, A.; Boucher, A. C.; Pastor, E.; Alonso-Vante, N. *Fuel Cells* **2002**, *2*, 109. (b) Boucher, A. C.; Alonso-Vante, N.; Dassenoy, F.; Vogel, W. *Langmuir* **2003**, *19*, 10885.
- (27) Yang, H.; Alonso-Vante, N.; Léger, J.-M.; Lamy, C. *J. Phys. Chem. B* **2004**, *108*, 1938.
- (28) Longoni, G.; Chini, P. *J. Am. Chem. Soc.* **1976**, *98*, 7225.
- (29) Calabrese, J. C.; Dahl, L. F.; Cavalieri, A.; Chini, P.; Longoni, G.; Martinengo, S. *J. Am. Chem. Soc.* **1974**, *96*, 2614.
- (30) (a) Gnatzmann, V.; Vogel, W. *J. Phys. Chem.* **1990**, *94*, 4991. (b) Vogel, W. *Cryst. Res. Technol.* **1998**, *33*, 1141.
- (31) Maillard, F.; Martin, M.; Gloaguen, F.; Léger, J.-M. *Electrochim. Acta* **2002**, *47*, 3431.
- (32) Pozio, A.; Francesco, M. D.; Cemmi, A.; Giorgi, L. *J. Power Sources* **2002**, *105*, 13.
- (33) (a) Miksa, D.; Brill, T. B. *Ind. Eng. Chem. Res.* **2001**, *40*, 3098. (b) Miksa, D.; Brill, T. B. *Ind. Eng. Chem. Res.* **2002**, *41*, 5151.
- (34) (a) Bengtsson-Kloo, L.; Iapalucci, M. C.; Longoni, G.; Ulvenlund, S. *Inorg. Chem.* **1998**, *37*, 4335. (b) Biani, F. F.; Femoni, C.; Iapalucci, M. C.; Longoni, G.; Zanello, P.; Ceriotti, A. *Inorg. Chem.* **1999**, *38*, 3721.
- (35) Borodzinski, A.; Bonarowska, M. *Langmuir* **1997**, *13*, 5613.
- (36) Antolini, E. *Mater. Chem. Phys.* **2003**, *78*, 563.
- (37) Esch, U.; Schneider, A. *Z. Elektrochem.* **1944**, *50*, 268.
- (38) Solliard, F. *Surf. Sci.* **1985**, *156*, 484.
- (39) Vogel, W.; Bradley, J.; Vollmer, O.; Abraham, I. *J. Phys. Chem. B* **1998**, *102*, 10853.
- (40) Vogel, W.; Britz, W.; Bönnemann, P.; Rothe, H.; Hormes, J. *J. Phys. Chem. B* **1997**, *107*, 11029.
- (41) Hartmann, N.; Imbihl, R.; Vogel, W. *Catal. Lett.* **1994**, *28*, 373.
- (42) Reetz, M. T.; Lopez, M.; Grüner, W.; Vogel, W.; Mahlendorf, F. *J. Phys. Chem. B* **2003**, *107*, 7414.
- (43) Matyi, R. J.; Schwartz, L. H.; Butt, J. B. *Catal. Rev.—Sci. Eng.* **1987**, *29*, 41.
- (44) Anderson, A. *Electrochim. Acta* **2002**, *47*, 3759.
- (45) Schmidt, T. J.; Paulus, U. A.; Gasteiger, H. A.; Alonso-Vante, N.; Behm, R. J. *J. Electrochem. Soc.* **2000**, *147*, 2620.
- (46) Markovic, N. M.; Ross, P. N. *Surf. Sci. Rep.* **2002**, *45*, 117.
- (47) Mukerjee, S.; McBreen, J. *J. Electrochem. Soc.* **1999**, *146*, 600.